

Synthesis and density-functional-theory calculations of electronic band structure of hollow sphere WS₂

MAXWELL SELASE AKPLE*, HOLALI KWAMI APEVIENYEKU

Mechanical Engineering Department, Ho Technical University, P.O. Box HP 217, Ho, Volta Region, Ghana

A novel and low-cost synthesis of tungsten disulfide (WS₂) transition metal dichalcogenide was carried out via gas-solid reaction in a horizontal quartz reactor. In this process, the prepared hollow WO₃ precursor was sulfided with CS₂ at 550 °C at different durations under N₂ gas atmosphere. The as-prepared WS₂ samples were formed by substitution of O by S during the sulfidation process. The characterization of these samples was performed employing X-ray diffraction (XRD), scanning electron microscopy (SEM), transmission electron microscopy (TEM), energy dispersive X-ray (EDX), Brunauer-Emmett-Teller (BET) specific surface area, X-ray photoelectron spectroscopy (XPS) and UV-Vis absorption spectroscopy. The characterization results showed that the as-prepared WS₂ samples were of high quality and purity. No significant differences were observed in various WS₂ samples synthesized during different sulfidation periods. The calculated results obtained from the density functional theory (DFT) indicate that WS₂ has an indirect band gap of ca. 1.56 eV, which is in agreement with experimental band gap of ca. 1.50 eV. Combining the experimental and DFT results suggests that the novel method used in the synthesis of WS₂ has a potential application for large scale production. The obtained WS₂ are of high quality and can be implemented in photocatalysis, catalysis, photovoltaics, optoelectronic devices and photosensor devices.

Keywords: *transition metal dichalcogenide; WS₂; DFT*

1. Introduction

Transition metal dichalcogenides (TMDCs) are the group of layered nanomaterials which have attracted a lot of interest in recent times. TMDCs are group IV-VII metals with the chemical structure like MX₂, where M is a transition metal atom (e.g. tungsten, molybdenum) and X is a chalcogen atom (e.g. S, Se, Te, etc.) [1, 2]. The X-M-X slab structure is built of two layers of carefully packed chalcogenide atoms sandwiching one metal layer between them. The slabs are stacked with only van der Waals forces. They exhibit semi-conducting, metallic and even superconducting behavior, hence, have a broad range of applications in nanoelectronics and optoelectronics [3–9]. The semiconducting phases of TMDCs, such as MoS₂, WS₂, WSe₂, MoSe₂ in the bulk form, have an indirect band gap [10, 11]. However, modification of the bulk properties into a mono- or few-layered structure could significantly change them into direct band gap [3]. These variations in the band

structure show potential application of the TMDCs in new structures development. These properties have drawn the attention of many scientists who are progressively studying the modifications of the TMDCs. According to the studies, many synthetic methods have been reported for the preparation of TMDCs including solid-gas or gas-phase reactions, electron beam irradiation activation and arc discharge, thermal decomposition, spray pyrolysis, hydrothermal or solvothermal synthesis, sono-electrochemical process and template synthesis [12–19].

Tungstenite or tungsten disulfide (WS₂) semiconductor material belongs to the TMDCs which have drawn the attention of researchers. In the bulk form, it has a band gap of ~1.3 eV, which is inactive because its redox potentials of photogenerated electrons and holes are not sufficient for the interfacial charge transfer onto adsorbed molecules for many photocatalytic applications [20]. However, this band gap can be tuned to more suitable values through quantum confinement effects for practical applications in photovoltaics and photocatalysis [11, 21]. Different approaches have been

*E-mail: makple@htu.edu.gh

suggested for the preparation and tuning of the crystal structure and the number of layers of WS₂. They included mechanical exfoliation, chemical vapor deposition (CVD), liquid exfoliation and sulfurization of transition metal and metal oxide [8, 22–26]. The WS₂ produced by these methods are slightly different in structure depending on the precursor(s) used and the rate of WS₂ formation [26]. Besides, some of these methods also use toxic and hazardous gasses such as H₂S which are difficult to handle and require high-temperature procedures which may result in cost increase and further limit the potential applications [17, 27]. Sun *et al.* [28] showed that for industrial production of WS₂, the most successful technique is the conversion of oxide-to-sulfide.

To obtain high-quality WS₂, the morphology of the oxide precursor is crucial. Hence, high-quality precursors which show unique plane structural defects are essential for the preparation of WS₂ with ordered and stacked layered structure. Herein, we report the synthesis of the hollow sphere WS₂ layered structure using a prepared solid WO₃ hollow sphere as a precursor. The synthesis method is simple, convenient and efficient, where the WO₃ hollow microsphere used as a precursor is placed in a horizontal tubular quartz reactor, and CS₂ vapor is passed through the system. The substitution of O by S along the (0 0 1) planes of WO₃ converts the WO₃ precursor to (0 0 2) WS₂ planes. This preparation technique has a potential for large scale production of WS₂ because of its simplicity, inexpensiveness, easy to control, and environmental friendliness. Further investigation into the electronic structure of bulk WS₂ was carried out from first-principles calculations using density functional theory (DFT). The acquired knowledge would provide an insight into the values which would enable practical synthesis and application of WS₂.

2. Experimental

2.1. Preparation of WO₃ hollow sphere

All chemicals were of analytical grade and used without further purification. The detailed experimental process for the preparation of WO₃ has been

reported in previous studies [29, 30]. Three starting aqueous solutions, SrCl₂ (0.1 mol/L), Na₂WO₄ (0.1 mol/L) and polymethacrylic acid (PMAA) (10 g/L) were prepared firstly. In a typical experiment, 10 mL of SrCl₂ solution (0.1 mol/L), 0.5 mL of PMAA solution (10 g/L) and 29.5 mL of distilled water were mixed in a beaker under magnetic stirring for 5 min. Then, 10 mL of Na₂WO₄ solution (0.1 mol/L) was slowly added under vigorous stirring, giving final concentrations of 0.02 mol/L for both Sr²⁺ and WO₄²⁻ and 0.1 g/L for PMAA. The starting pH value of the mixture was adjusted to 12 using 2 mol/L NaOH or HCl solution. After continuous vigorous stirring for 5 min, the mixture was sealed and incubated at room temperature for 12 h. The resulting white precipitate was washed with distilled water and ethanol, and dried in air. Tungsten oxide hydrate hollow microspheres were accomplished by soaking the as-prepared SrWO₄ samples in a concentrated HNO₃ solution (8 mol/L) at room temperature for 24 h, and then washing with distilled water and ethanol for three times, respectively. The washed precipitate was dried in a vacuum oven at 60 °C for 8 h and finally calcined at 300 °C for 2 h in air.

2.2. Preparation of WS₂ hollow sphere

A gas-solid reaction was performed under inert gas (nitrogen) to prepare the WS₂ samples. The prepared WO₃ was employed as tungsten precursor and CS₂ (ACS reagent >99.9 %, Sigma-Aldrich) as a sulfur source. In detail, 1.0 g of the prepared WO₃ hollow spheres was weighed and placed in a ceramic boat. The ceramic boat was positioned in a quartz tube furnace whose ends were equipped with high-temperature O-rings and stainless steel lids for gas introduction and exhaust. A gas purge step was performed to make sure that no oxygen was present inside the reactor. The quartz tube was then inserted into the clamp tubular furnace, and the temperature was raised to 550 °C at a heating rate of 5 °C min⁻¹, then the nitrogen gas with CS₂ vapor was introduced into the quartz tube for the reaction to occur at different durations of 1 h, 2 h and 3 h. After the reaction time was over, the powder was allowed to cool under the gas and then it was

subjected to further characterization. The samples were labeled WO_3 , WS_2 -1, WS_2 -2 and WS_2 -3 to denote the sulfidation period of 0 h, 1 h, 2 h, and 3 h, respectively.

2.3. Characterization

Powder X-ray diffraction (XRD) investigations were conducted on an X-ray diffractometer (Rigaku, Japan) using $\text{CuK}\alpha$ irradiation ($\lambda = 0.15418$ nm) at a scan rate of $0.05^\circ/\text{s}$. Transmission electron microscopy (TEM) and high-resolution transmission electron microscopy (HRTEM) analyses were conducted using a JEM-2100F electron microscope (JEOL, Japan). The element distribution mapping measurement was performed on an S4800 field emission scanning electron microscope (FE-SEM, Hitachi, Japan) equipped with an X-Max 50 energy-dispersive X-ray spectroscopy (EDS, Oxford Instruments, Britain) with an accelerating voltage of 10 kV. The Brunauer-Emmett-Teller (BET) specific surface area (S_{BET}) of the samples was determined by nitrogen adsorption data in a Micromeritics ASAP 2020 nitrogen adsorption apparatus (USA). All the samples were degassed at 180°C before the nitrogen adsorption measurements. A desorption isotherm was used to determine the pore size distribution by the Barret-Joyner-Halender (BJH) method, using a cylindrical pore model [31]. The nitrogen adsorption volume at the relative pressure (P/P_0) of 0.99 was used to calculate the pore volume and average pore size. X-ray photoelectron spectroscopy (XPS) measurements were done by using an ultrahigh vacuum VG ESCALAB 210 electron spectrometer equipped with a multichannel detector, using $\text{MgK}\alpha$ (1253.6 eV) radiation (operated at 200 W) of a twin anode in a constant analyzer energy mode with a pass energy of 30 eV. All the binding energies were referenced to the C 1s peak at 284.8 eV of the surface adventitious carbon. The optical absorption properties of the samples were obtained with a UV-Vis absorption spectrophotometer (UV-2600, Shimadzu, Japan). BaSO_4 was used as a reflectance standard in the UV-Vis reflectance experiment.

2.4. DFT computational details

The energy calculations were based on DFT using the CASTEP code with the plane-wave pseudopotential method [32]. The exchange-correlation function based on generalized gradient approximation (GGA) with the Perdew-Burke-Ernzerhof (PBE) was used. The interaction between valence electrons and the ionic core was described by the ultrasoft pseudopotential [33, 34]. The atomic coordinates and lattice parameters were relaxed by the cutoff of 460 eV and Monkhorst-Pack grids of $9 \times 9 \times 2$ k-points. Other convergence tolerance parameters used for geometry optimization calculations were a total energy of 1×10^{-5} eV per atom, maximum force 0.03 eV per \AA , a maximum stress of 0.05 GPa and a maximum atomic displacement of 0.001 \AA . The valence electron configurations of $\text{W-}5s^25p^65d^46s^2$ and $\text{S-}3s^23p^4$ were used for the bulk WS_2 calculation, while the inner electrons were kept frozen as core states. Higher cutoff energy and denser k-point grids cannot obviously change the energy and the geometry structure of WS_2 . After finishing the geometry optimization, the band structures and density of state (DOS) of the bulk WS_2 were calculated.

3. Results and discussion

3.1. Morphology and phase microstructure analysis

The SEM images of both the synthesized pure WO_3 and WS_2 samples are shown in Fig. 1. Sulfidation process was used to convert the prepared WO_3 into WS_2 . The morphology of the WO_3 resembles a hollow in nature microsphere with the diameter of 2 μm to 4 μm . It can be seen that after the sulfidation process at different durations, the WO_3 precursor and the WS_2 samples have similar morphologies, suggesting that WS_2 preparation process (i.e. sulfidation) did not affect the morphology of the WO_3 precursor. It was also evidenced by the low magnification TEM micrographic studies (Fig. 2a). From the HRTEM images presented in Fig. 2b and Fig. 2c, onion-like layers with crystal lattice fringes spacing of ca. 0.62 nm, corresponding to the (0 0 2) plane of 2H- WS_2 have been

revealed [35, 36]. These images suggest that there is the dominance of layered arrays in the structure which is characteristic of WS_2 . EDX elemental mapping was carried out to determine the presence of all the elements in the as-prepared WS_2 sample. Fig. 3 shows the mapping images obtained where only W and S elements were detected. Besides, the quantitative analysis of elements based on the EDS result was performed and W:S atomic ratio was calculated to be 1.1:2.3 which is close to the stoichiometric ratio of 1:2. Based on this study, it is clear that WS_2 has been synthesized.

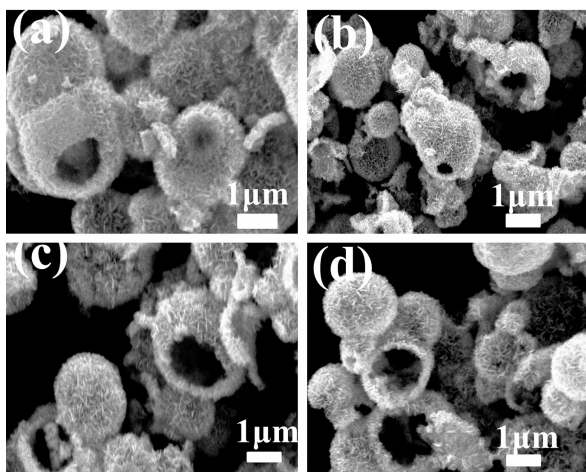


Fig. 1. SEM images for pure WO_3 (a), WS_2 -1 (b), WS_2 -2 (c), and WS_2 -3 (d).

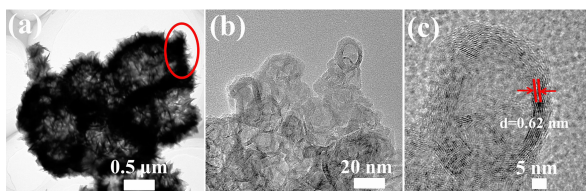


Fig. 2. (a) TEM image; (b) and (c) HRTEM images of WS_2 -3 sample.

XRD analysis was carried out to show the phase structures of the pure WO_3 precursor and the as-prepared WS_2 samples. Fig. 4 shows the XRD pattern of the pure WO_3 before and after the sulfidation period (i.e. for WS_2 samples). The diffraction peaks of the WO_3 XRD pattern can be indexed to the pure monoclinic phase of WO_3 (JCPDS Card

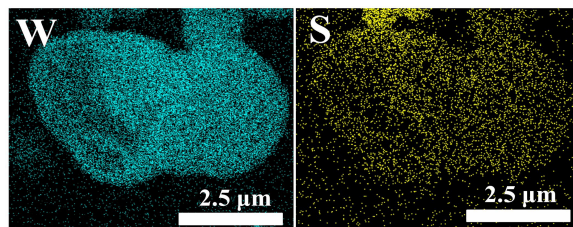


Fig. 3. EDX elemental mapping for WS_2 -3 sample showing W and S elements.

No. 72-1465, $a = 7.3 \text{ \AA}$, $b = 7.53 \text{ \AA}$, $c = 7.68 \text{ \AA}$). The XRD patterns of the as-prepared WS_2 samples differ from that of the WO_3 precursor suggesting phase change during the sulfidation process. It can be seen that after 1 h sulfidation process, all WO_3 peaks completely disappeared resulting in the appearance of peaks corresponding to WS_2 , which confirms that the S atom from the CS_2 gas has started replacing the O atoms in the WO_3 , resulting in the partial formation of WS_2 . Notably, among them a diffraction peak at 13.9° corresponding to (0 0 2) plane has appeared which is an indication of the WS_2 layer or coating formation on the precursor. Further increase in the sulfidation period resulted in higher WS_2 peak intensities and showed completed structure after 3 h sulfidation period. It can be observed from Fig. 4b that the XRD pattern of as-prepared WS_2 samples matches the pure crystal phase of hexagonal WS_2 structure which is indexed to PDF Card No. 35-0651. The intense peak at 13.9° corresponding to (0 0 2) plane indicates the formation of well-stacked layered WS_2 structure. This result is in agreement with other previous studies [11, 20, 37].

3.2. BET surface area and pore size distribution

The nitrogen adsorption-desorption isotherms of the pure WO_3 and the WS_2 as-prepared samples are shown in Fig. 5. Both samples exhibit isotherms of type IV BDDT (Brunauer-Deming-Deming-Teller) classification suggesting bimodal pore size distribution in the mesoporous and macroporous regions. The hysteresis loops in relatively lower pressure range ($0.5 < P/P_0 < 0.8$) are associated with finer intra-aggregated pores

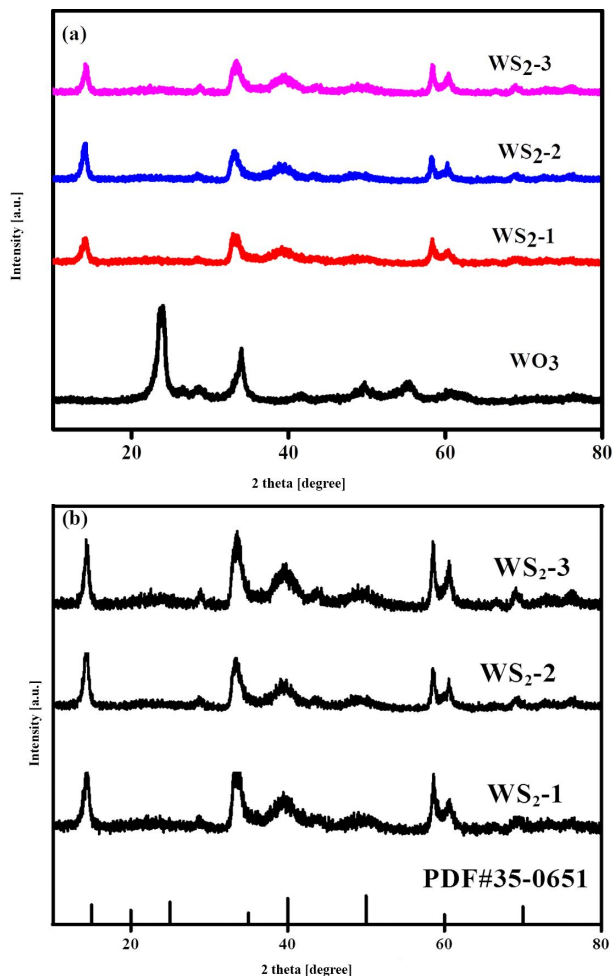


Fig. 4. (a) XRD patterns of pure WO_3 and WS_2 at different sulfidation times; (b) comparison of XRD patterns of as-prepared WS_2 samples and PDF Card No. 35-0651.

in the agglomerated particles while in the higher relative pressure range ($0.8 < P/P_0 < 1$), it is related with larger inter-aggregated pores between the aggregated particles [30]. The presence of the bimodal pore in the as-prepared samples was further confirmed by the pore-size distribution curves shown as an inset in Fig. 5. The BJH (Barrett-Joyner-Halenda) method was employed to determine the desorption branch of the nitrogen isotherm. The pore size distribution shows a broad range of pore size diameters from 2 nm to 130 nm. The WS_2 as-prepared sample has small mesopores (peak pores at 2.5 nm and 3.6 nm) and macropores (peak pore at 45 nm), while

the WO_3 shows the peak pore of large mesopores at ca. 11 nm and macropores at 25 nm. Table 1 illustrates the summary of physical properties of the as-prepared samples. It can be observed that the WS_2 has a larger surface area, pore volume, and pore size compared to the WO_3 precursor. The increase in these properties could be ascribed to the formation of WS_2 layers on the surface of the precursor.

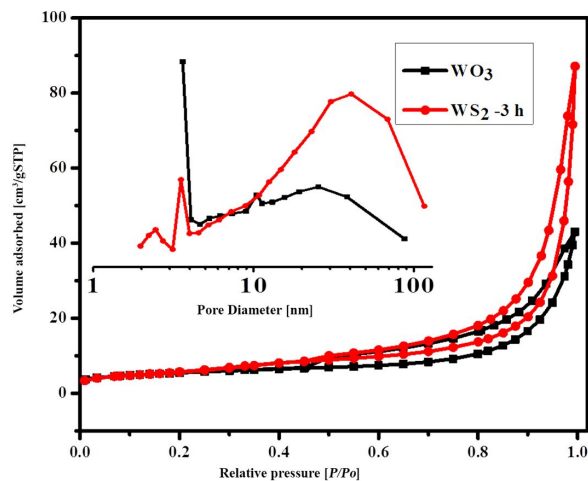


Fig. 5. Nitrogen adsorption isotherms of WO_3 and as-prepared WS_2 -3. The inset shows the pore size distribution curves.

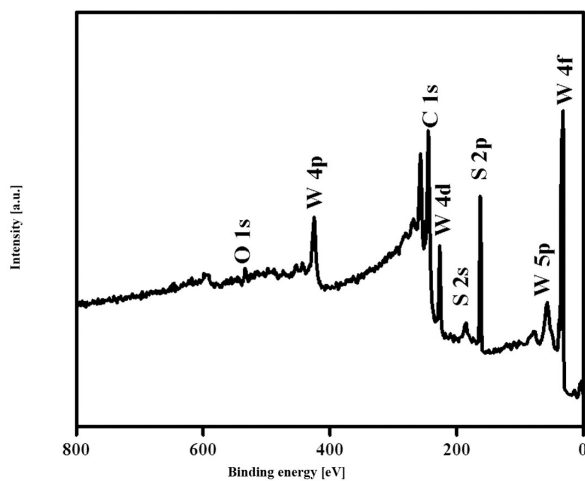
3.3. XPS analysis

To further determine the chemical composition and the oxidation states of the elements in the as-prepared WS_2 samples, XPS analysis was carried out. The survey spectrum shows the presence of O, C, S, and W in the WS_2 prepared samples (Fig. 6). It can be seen from the spectrum that W and S elements have sharp peaks at 33.1 eV and 161.2 eV binding energy, respectively, with small peaks for C and O. The carbon peak (C 1s 285 eV) is attributed to surface adventitious carbon which comes from the sample and the XPS instrument itself. The oxygen peak (O 1s 532 eV) could come from adsorbed water molecules on the surface of the sample.

Fig. 7a illustrates the high-resolution spectrum of W 4f showing two core peaks with binding energies at 32.2 eV and 34.2 eV for $4f_{7/2}$ and $4f_{5/2}$, respectively. These peaks can be ascribed to the W^{4+}

Table 1. Summary of the physical properties of the WO_3 and WS_2 -3 h samples.

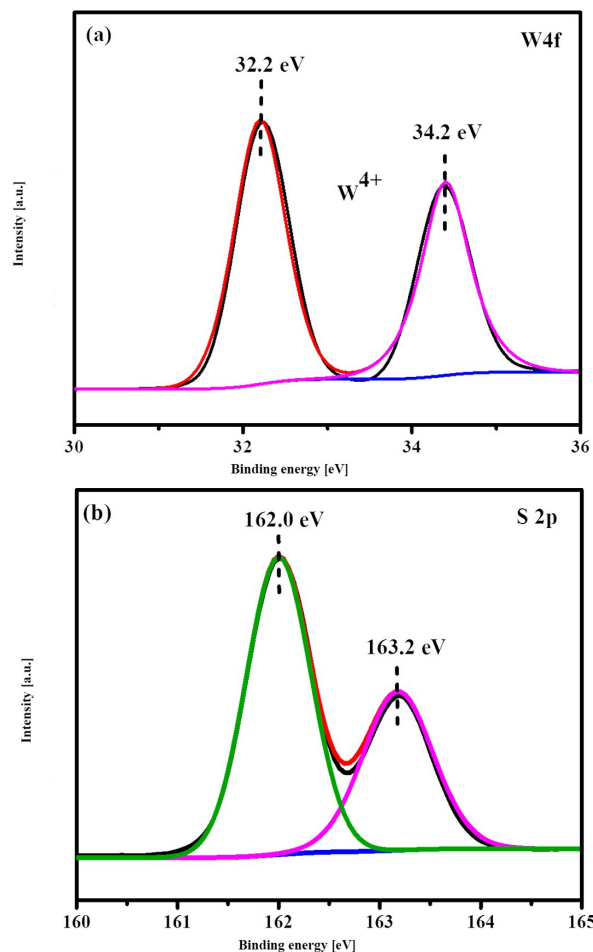
Sample	S_{BET} [m^2/g]	Pore volume [cm^3/g]	Average pore size [nm]
WO_3	19.3	0.05	10.0
WS_2 -3	20.3	0.07	14.0

Fig. 6. Survey spectrum of the as-prepared WS_2 sulfided for 3 h.

species in the as-prepared samples [36, 38]. The high-resolution spectrum of the S 2p core region has two characteristic peaks at binding energies of 162.0 eV and 163.2 eV for $2p_{3/2}$ and $2p_{1/2}$, respectively. These peaks correspond to S^{2-} species in the samples [25]. Combining this result with the W 4f spectrum, confirms the formation of WS_2 .

3.4. UV-Vis spectra and optical properties

The light harvesting or optical properties of the as-prepared WS_2 samples was characterized by UV-Vis absorption spectroscopy. The UV-Vis spectra of the WO_3 precursor and as-prepared WS_2 samples are shown in Fig. 8a. It can be seen that the WO_3 has an absorption edge at ~ 468 nm which corresponds to the band gap of 2.65 eV and agrees with previous studies [30, 39]. The as-prepared WS_2 samples display an extended absorption to 820 nm corresponding to the bandgap of ~ 1.5 eV as shown in Fig. 8b. According to the literature, bulk WS_2 has the absorption edge at ~ 920 nm (1.35 eV bandgap), so the bandgap of ~ 1.5 eV is an indication of large blue shift for the as-prepared

Fig. 7. High-resolution XPS spectra; (a) W 4f and (b) S 2p of as-prepared WS_2 sample sulfided for 3 h.

WS_2 samples due to strong quantum confinement effect in the samples. This quantum confinement effect leads to an increase in the band gap and a change in redox potential [10, 25]. The spectra of the as-prepared WS_2 samples also show a characteristic A-B excitonic peak positions at the wavelengths 616 nm and 513 nm which correspond to 2.0 eV and 2.4 eV band gaps, respectively. The excitonic peaks are related to direct strong valence band spin-orbit splitting at the Brillouin zone

K point [11, 25, 40] and is present only in the bulk WS_2 , which further confirms the formation of bulk WS_2 .

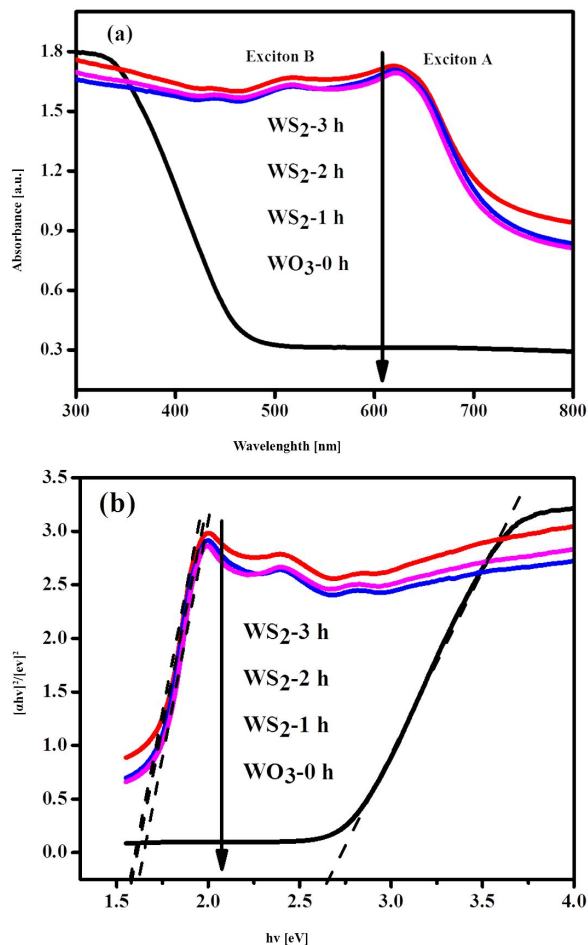


Fig. 8. (a) UV-Vis diffuse reflection spectra; (b) Kubelka-Munk function for band gap energies of the as-prepared samples.

3.5. Electronic structure

Fig. 9 shows the conventional unit cell of bulk WS_2 respectively, which have 2H polytype crystalline system with hexagonal symmetry and space group $P63/mmc$ (D_{6h}^4). The experimental lattice parameters used in this study were ($a = b = 3.153 \text{ \AA}$, $c = 12.323 \text{ \AA}$, and $\alpha = \beta = 90^\circ$, $\gamma = 120^\circ$) [41, 42]. DFT was used to perform geometry optimization for the lattice parameters before calculating the electronic structures. The obtained optimized lattice

constants are $a = b = 3.184 \text{ \AA}$, $c = 14.297 \text{ \AA}$, and $\alpha = \beta = 90^\circ$, which shows slight overestimation relative to the experimental results, which is due to the shortcoming of exchange-correlation function of GGA. The percentage deviations between the calculated and experimental values are within 2.0 %, which is an indication of sufficient accuracy in the pseudopotential used for the calculations.

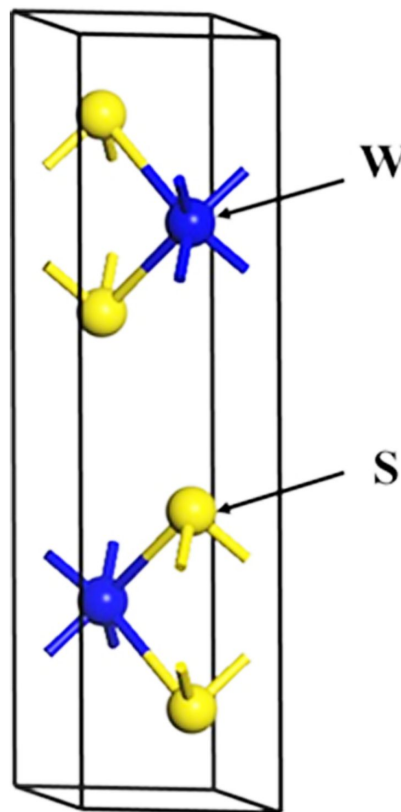


Fig. 9. A schematic conventional unit cell of hexagonal phase WS_2 .

To clarify the underlying electronic properties of WS_2 , the band structures of WS_2 along the high symmetry directions were calculated and shown in Fig. 10. The dashed line shows the Fermi level which was set at zero. It can be seen that the valence bands of WS_2 can be divided into four band regions (Fig. 10a). The conduction band minimum (CBM) is located at Z point, while the valence band maximum (VBM) is located at G point, which confirms that the WS_2 is an indirect band gap semiconductor. The difference between the bands

leads to a conclusion that there is an energy gap between the conduction and valence band at the Fermi level which is determined to be about 1.56 eV (Fig. 10b). It is in a good agreement with other calculated results [43, 44]. The band gap obtained for the as-prepared WS₂ samples is ~1.5 eV (Fig. 8), further indicating the reliability of the DFT calculation.

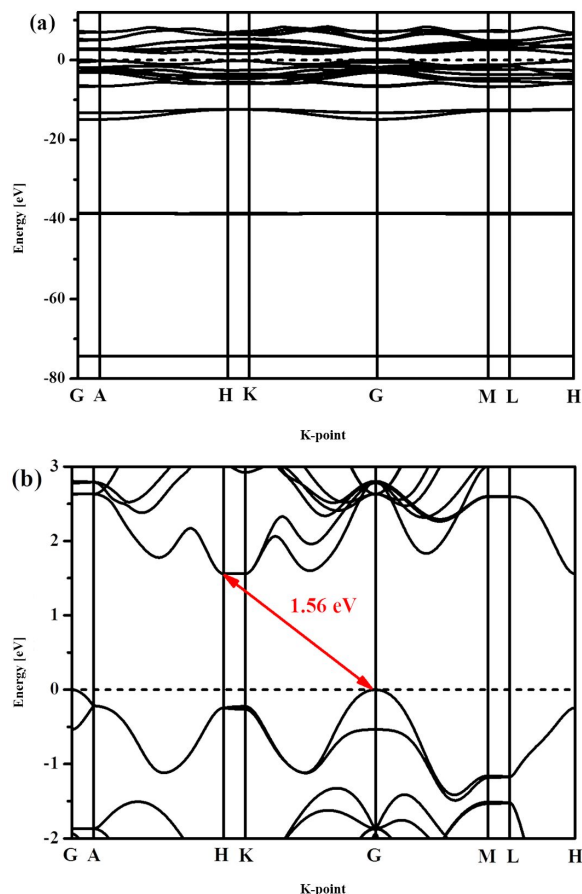


Fig. 10. (a) The band structures of WS₂ and (b) a magnified band structure around the Fermi level.

To further understanding the composition and nature of the band structures, the TDOS of WS₂ and PDOS of W and S have been calculated and shown in Fig. 11. The valence bands at -74.0 eV and -38.0 eV correspond to W 6s and W 5p states, respectively. The valence bands between -15 eV and -11 eV are mainly contributed by S 3s states and a few W 6s, 5d states. The upper valence bands between -7.0 eV and 0 eV are mainly contributed

by S 3p states and a few W 5d states. However, the conduction band is mainly composed by W 5d states, mixed with a few S 3p states. This suggests the existence of strong p-d hybridization between S atoms and W states in the valence and conduction bands. These observations agree well with other previous reports [45].

4. Conclusions

WS₂ was successfully prepared via a gas-solid reaction where WO₃ precursor was sulfided with CS₂ at 550 °C at different durations under N₂ inert gas atmosphere. The reaction occurred by substitution of O by S during the sulfidation process. Characterization of the as-prepared WS₂ samples confirmed the formation of WS₂ in the appropriate stoichiometric ratio. The calculated results indicate

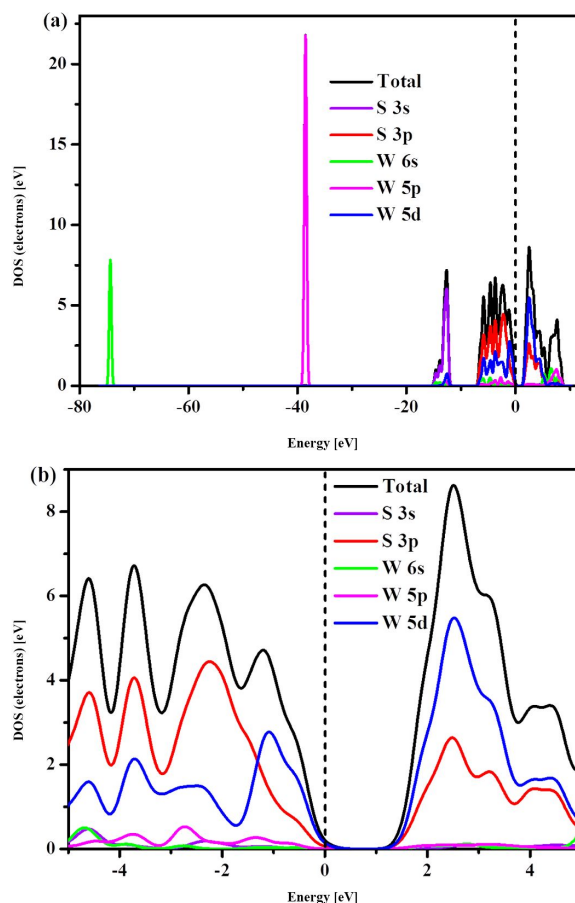


Fig. 11. (a) The DOS of WS₂ and (b) the magnified DOS around the Fermi level.

that WS₂ has an indirect band gap of ca. 1.56 eV, which is very close to the experimental band gap of ca. 1.50 eV. Combining the experimental and DFT results suggests that the novel method used in the synthesis of WS₂ has a potential application for large scale production. The obtained WS₂ are of high quality, presenting appropriate properties for applications in photocatalysis, catalysis, photovoltaics, optoelectronic devices and photosensor devices.

Acknowledgements

The authors would like to acknowledge the financial support from the Ghana Government Book and Research Allowance for tertiary institutions. We also acknowledge contributions from members of the Mechanical Engineering Department of the Ho Technical University, Ghana, and the State Key Laboratory of Advanced Technology for Material Synthesis and Processing, Wuhan University of Technology, Wuhan 430070, P.R. China, for supporting the research in diverse ways.

References

- [1] CHEN S.Y., ZHENG C., FUHRER M.S., YAN J., *Nano Lett.*, 15 (2015), 2526.
- [2] WANG Y., CONG C., YANG W., SHANG J., PEIMYOO N., CHEN Y., KANG J., WANG J., HUANG W., YU T., *Nano Res.*, (2015), 1.
- [3] WANG Q.H., KALANTAR-ZADEH K., KIS A., COLEMAN J.N., STRANO M.S., *Nat. Nanotechnol.*, 7 (2012), 699.
- [4] ZHAN Y., LIU Z., NAJMAEI S., AJAYAN P.M., LOU J., *Small*, 8 (2012), 966.
- [5] ZENG H., DAI J., YAO W., XIAO D., CUI X., *Nat. Nanotechnol.*, 7 (2012), 490.
- [6] GHOREISHI S., MESHKAT S., DADKHAH A., *Mater. Res. Bull.*, 45 (2010), 584.
- [7] CHOU S.S., HUANG Y.K., KIM J., KAEHR B., FOLEY B.M., LU P., DYKSTRA C., HOPKINS P.E., BRINKER C.J., HUANG J., *J. Am. Chem. Soc.*, 137 (2015), 1742.
- [8] LUKOWSKI M.A., DANIEL A.S., ENGLISH C.R., MENG F., FORTICAUX A., HAMERS R. J., JIN S., *Eng. Environ. Sci.*, 7 (2014), 2608.
- [9] PARK J., LEE W., CHOI T., HWANG S. H., MYOUNG J.M, JUNG J. H, KIM S. H, KIM H., *Nanoscale*, 7 (2015), 1308.
- [10] ELÍAS A. L., PEREA-LÓPEZ N., CASTRO-BELTRÁN A., BERKDEMIR A., LV R., FENG S., LONG A. D., HAYASHI T., KIM Y. A., ENDO M., *ACS Nano*, 7 (2013), 5235.
- [11] NOTLEY S.M., *J. Colloid Interf. Sci.*, 396 (2013), 160.
- [12] CHEN D., TANG K., SHEN G., SHENG J., FANG Z., LIU X., ZHENG H., QIAN Y., *Mater. Chem. Phys.*, 82 (2003), 206.
- [13] ELLMER K., *Phys. Status Solidi B*, 245 (2008), 1745.
- [14] HOU X., SHAN C., CHOY K.L., *Surf. Coat. Technol.*, 202 (2008), 2287.
- [15] MARGOLIN A., DEEPAK F., POPOVITZ-BIRO R., BAR-SADAN M., FELDMAN Y., TENNE R., *Nanotechnology*, 19 (2008), 095601.
- [16] WU J., FU X., *Mater. Lett.*, 61 (2007), 4332.
- [17] WIESEL I., ARBEL H., ALBU-YARON A., POPOVITZ-BIRO R., GORDON J.M., FEUERMAN D., TENNE R., *Nano Res.*, 2 (2009), 416.
- [18] WEN Y., ZHANG H., ZHANG S., *Nanoscale*, 6 (2014), 13090.
- [19] CHOI S.H., BOO S.J., LEE J. H., KANG Y.C., *Sci. Rep.-UK*, 4 (5755) (2014), 4.
- [20] JAMES D., ZUBKOV T., *J. Photoch. Photobio. A*, 262 (2013), 45.
- [21] CAO S., LIU T., HUSSAIN S., ZENG W., PAN F., PENG X., *J. Mater. Sci.-Mater. El.*, 26 (2015), 809.
- [22] THANGARAJA A., SHINDE S.M., KALITA G., TANEMURA M., *Mater. Lett.*, 156 (2015), 156.
- [23] YANG J., VOIRY D., AHN S.J., KANG D., KIM A.Y., CHHOWALLA M., SHIN H.S., *Angew. Chem. Int. Edit.*, 52 (2013), 13751.
- [24] CHHOWALLA M., SHIN H.S., EDA G., LI L.J., LOH K.P., ZHANG H., *Nat. Chem.*, 5 (2013), 263.
- [25] MORRISH R., HAAK T., WOLDEN C.A., *Chem. Mater.*, 26 (2014), 3986.
- [26] TEHRANI M., LUHRS C., AL-HAIK M., TREVINO J., ZEA H., *Nanotechnology*, 22 (2011), 285714.
- [27] CAO S., LIU T., HUSSAIN S., ZENG W., PENG X., PAN F., *Mater. Lett.*, 129 (2014), 205.
- [28] SUN S., ZOU Z., MIN G., *Mater. Chem. Phys.*, 114 (2009), 884.
- [29] ZHAO X., CHEUNG T.L., ZHANG X., NG D.H., YU J., *J. Am. Ceram. Soc.*, 89 (2006), 2960.
- [30] YU J., QI L., CHENG B., ZHAO X., *J. Hazard. Mater.*, 160 (2008), 621.
- [31] SING K.S., *Pure Appl. Chem.*, 57 (1985), 603.
- [32] SEGALL M., LINDAN P.J., PROBERT M.A., PICKARD C., HASNIP P., CLARK S., PAYNE M., *J. Phys. Condens. Mat.*, 14 (2002), 2717.
- [33] PERDEW J. P., BURKE K., ERNZERHOF M., *Phys. Rev. Lett.*, 77 (1996), 3865.
- [34] PERDEW J. P., WANG Y., *Phys. Rev. B*, 45 (1992), 13244.
- [35] HOU Y., LAURSEN A.B., ZHANG J., ZHANG G., ZHU Y., WANG X., DAHL S., CHORKENDORFF I., *Angew. Chem., Int. Edit.*, 52 (2013), 3621.
- [36] YANG L., ZHOU H., FAN T., ZHANG D., *PCCP*, 16 (2014), 6810.
- [37] WU Z., WANG D., ZAN X., SUN A., *Mater. Lett.*, 64 (2010), 856.
- [38] ZONG X., HAN J., MA G., YAN H., WU G., LI C., *J. Phys. Chem. C*, 115 (2011), 12202.
- [39] JIN J., YU J., GUO D., CUI C., HO W., *Small*, 11 (2015), 5262.

- [40] RODRIGUEZ GUTIERREZ H., PEREA-LÓPEZ N., ELÍAS A. L., BERKDEMIR A., WANG B., LV R., LÓPEZ-URÍAS F., CRESPI V., TERRONES H., TERRONES M., *J. APS*, March Meeting Abstracts, (2013), 5007.
- [41] WILSON J., YOFFE A., *Adv. Phys.*, 18 (1969), 193.
- [42] KUC A., ZIBOUCHE N., HEINE T., *Phys. Rev. B*, 83 (2011), 245213.
- [43] SAYAN R., PETER B., *Sol. Energ. Mat. Sol. C.*, 174 (2018), 370.
- [44] FORTI S., ROSSI A., BÜCH H., CAVALLUCCI T., BISIO F., SALA A., MENTEŞ T. O., LOCATELLI A., MAGNOZZI M., CANEPA M., MÜLLER K., LINK S., STARKE U., TOZZINIB V., COLETT C., *Nanoscale*, 9 (2017), 16412.
- [45] KUMAR A., AHLUWALIA P., *Eur. Phys. J. B*, 85 (2012), 1.

Received 2017-05-17

Accepted 2018-03-15